Label-Free Live-Cell Imaging of Nucleic Acids Using Stimulated Raman Scattering Microscopy

Xu Zhang,[a, b] Maarten B. J. Roeffaers,[a, c] Srinjan Basu,[a, d] Joseph R. Daniele,[a, d] Dan Fu,[a] Christian W. Freudiger,[a] Gary R. Holtom,[a] and X. Sunney Xie*[a]

Imaging of nucleic acids is important for studying cellular processes such as cell division and apoptosis. A noninvasive label-free technique is attractive. Raman spectroscopy provides rich chemical information based on specific vibrational peaks. However, the signal from spontaneous Raman scattering is weak and long integration times are required, which drastically limits the imaging speed when used for microscopy. Coherent Raman scattering techniques, comprising coherent anti-Stokes Raman scattering (CARS) and stimulated Raman scattering (SRS) microscopy, overcome this problem by enhancing the signal level by up to five orders of magnitude. CARS microscopy suffers from a nonresonant background signal, which distorts Raman spectra and limits sensitivity. This makes CARS imaging of weak transitions in spectrally congested regions challenging. This is especially the case in the fingerprint region, where nucleic acids show characteristic peaks. The recently developed SRS microscopy is free from these limitations; excitation spectra are identical to those of spontaneous Raman and sensitivity is close to shot-noise limited. Herein we demonstrate the use of SRS imaging in the fingerprint region to map the distribution of nucleic acids in addition to proteins and lipids in single salivary gland cells of Drosophila larvae, and in single mammalian cells. This allows the imaging of DNA condensation associated with cell division and opens up possibilities of imaging such processes in vivo.

1. Introduction

Optical microscopy techniques are often required when studying cellular processes because they provide information on the distribution and dynamics of different biomolecules at the cellular level. Fluorescence microscopy has contributed greatly to our understanding of these processes. However, it relies on the use of fluorescent labels or dyes. These labels may be toxic or perturbative to cells, and are subject to photobleaching. It is therefore difficult to use them for studying long-term biological dynamics within living cells. Non-invasive label-free imaging techniques are desirable because they would allow long time observations without photobleaching in living cells or tissue where labeling is not always possible.

Raman microscopy is a label-free imaging technique that offers contrast based on vibrational frequencies that are characteristic of chemical bonds. It is therefore useful in determining the distribution of chemical components within a cell. Furthermore, it can be used to study the large-scale reorganization of these molecules that occur during cellular processes such as cell division, cell differentiation and apoptosis.[1,2] These processes involve the redistribution of lipids, proteins and nucleic acids, all of which have characteristic vibrational signatures in Raman spectra. It is therefore possible to use Raman microscopy to study them. However, spontaneous Raman scattering has very weak signals, so a long integration time is required to achieve a good signal to noise ratio (SNR).[3–5] This is not ideal for live cell imaging because biological dynamics generally occur at shorter time scales.

Coherent Raman scattering techniques, such as coherent anti-Stokes Raman scattering (CARS)[6–10] and stimulated Raman scattering (SRS),[11–15] can increase the speed of Raman imaging by up to five orders of magnitude. However, CARS microscopy contains a nonresonant background which distorts the Raman spectra[8] and limits the sensitivity.[9] This is particularly problematic when imaging below 1800 cm^{-1}, the vibrational fingerprint region, because this region has many neighboring peaks and these peaks have low intensities. Although CARS microspectroscopy with maximum entropy method (MEM) analyses has been used to circumvent this problem,[16] it is fair to say that CARS microscopy to date has focused predominantly on

[a] X. Zhang,+ Dr. M. B. J. Roeffaers,+ S. Basu,+ J. R. Daniele, Dr. D. Fu, Dr. C. W. Freudiger, Dr. G. R. Holtom, Prof. X. S. Xie
Department of Chemistry and Chemical Biology
Harvard University, 12 Oxford Street
Cambridge, MA 02138 (USA)
E-mail: xie@chemistry.harvard.edu

[b] X. Zhang+
School of Engineering and Applied Sciences
Harvard University, 29 Oxford Street
Cambridge, MA 02138 (USA)

[c] Dr. M. B. J. Roeffaers+
Department of Molecular and Microbial Systems
Katholieke Universiteit Leuven, Kasteelpark Arenberg 23
3001 Heverlee (Belgium)

[d] S. Basu,+ J. R. Daniele
Department of Molecular and Cellular Biology
Harvard University, 16 Divinity Avenue
Cambridge, MA 02138 (USA)

[+] These authors contributed equally to this work.

Supporting information for this article is available on the WWW under
http://dx.doi.org/10.1002/cphc.201100890.

the chemical imaging of C−H vibrations.[8] Recently, SRS microscopy has superseded CARS microscopy.[11–15] Free from the nonresonant background and spectral distortion, SRS signal is linearly proportional to the target molecule concentration and offers easy explanation of imaging contrast. Recently in vivo SRS imaging with video-rate imaging speed (30 frames s^{-1}) with signal collection in reflection of thick, non-transparent samples (epi-detection) was demonstrated[15]. SRS microscopy is particularly suited for imaging in the fingerprint region.

Imaging of nucleic acids that have vibrations within the fingerprint region has not been shown with SRS microscopy because of their much weaker signal compared to lipids. Nucleic-acid distributions are important for studying cellular processes such as cell division or apoptosis. The ability to detect these processes is useful for screening chemicals during drug discovery and for monitoring the growth of engineered tissues.[17] Herein, we demonstrate SRS imaging of the distribution of nucleic acids in living cells in addition to lipids and proteins. We show live cell imaging of single polytene chromosomes within the salivary glands of the fruit fly (Drosophila melanogaster), as well as imaging of two mammalian cell lines: human embryonic kidney cells (HEK-293) and breast cancer cells (MCF-7).

2. Results and Discussion

2.1. SRS Instrumentation

SRS is implemented with high-frequency modulation excitation and a high-frequency phase-sensitive detection scheme (Figure 1). Two excitation beams with the frequency difference matching the vibrational frequency of targeted molecules are utilized. The Stokes beam is provided by a 1064 nm Nd:YVO$_4$ laser (picoTRAIN, High-Q, Germany) which delivers a 6 ps pulse train at a 76 MHz repetition rate. The pump beam is provided by the signal output of an optical parametric oscillator (OPO) (Levante Emerald, APE-Berlin, Berlin, Germany) synchronously pumped by the frequency doubled Nd:YVO$_4$ laser at 532 nm. The wavelength of the pump beam can be tuned between 680 nm and 1010 nm.

The pump beam and the modulated Stokes beam are spatially overlapped using a dichroic mirror (1064DCRB, Chroma Technology, Bellow Falls, Vermont) and also temporally overlapped by adjusting a manual delay stage.

After transmission through an upright Olympus laser scanning microscope (BX61WI/FV300, Olympus, Pittsburgh, Pennsylvania), the excitation beams are focused onto the sample by a water immersion objective (UPlanApo/IR 60×/1.2 NA Olympus). A 1.45 NA oil immersion condenser is used to collect the transmitted light. A high NA condenser is used to reduce a potential artifact coming from cross phase modulation (XPM), which will be discussed in detail later in section 2.4.

In the SRS process, an increase in the intensity of the Stokes beam (stimulated Raman gain) occurs along with a decrease in the intensity of the pump beam (stimulated Raman loss). Since the intensity change is minute compared to the excitation beam intensity and can be buried within the laser noise, high-frequency intensity modulation at 10.4 MHz is applied to one
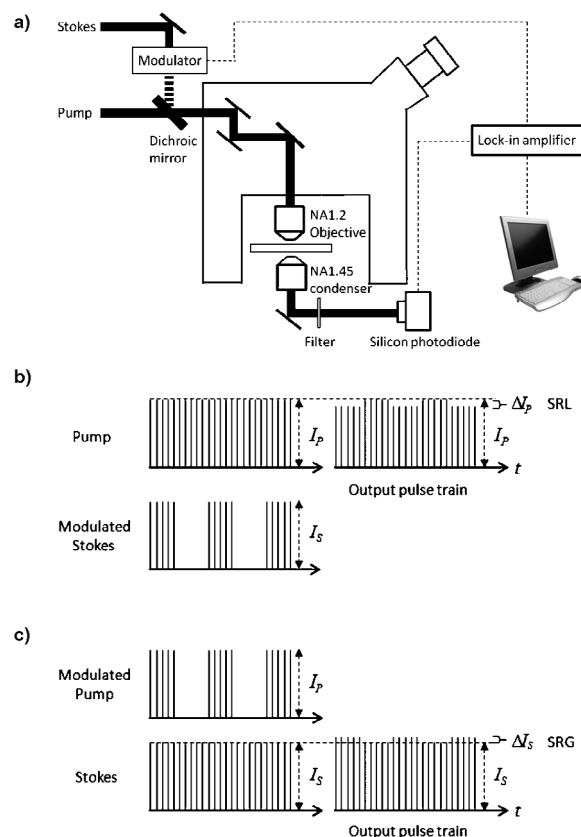
Figure 1. a) Experimental setup of the stimulated Raman loss (SRL) microscope. For SRG, the pump beam is modulated instead of the Stokes beam and an InGaAs photodetector is used instead of a silicon photodetector because of its better reponsivity at 1064 nm. b) Detection scheme of SRL. The Stokes beam is modulated at 10.4 MHz, where the resulting amplitude modulation of the pump beam due to the stimulated Raman loss can be detected. c) Detection scheme of SRG. The pump beam is modulated at 10.4 MHz, where the resulting amplitude modulation of the Stokes beam due to the stimulated Raman gain can be detected.

of the excitation beams so that the SRS signal can be separated from the laser noise, which occurs at much lower frequencies, using lock-in detection (SR844RF, Stanford Research Systems, Sunnyvale, California). In the stimulated Raman loss detection scheme (Figure 1 a, b), the Stokes beam is modulated at 10.4 MHz and the transmitted pump beam is detected using a 1 cm^2 silicon photodiode with a reverse bias of 64 V to 128 V after filtering out the Stokes beam using a bandpass filter (CARS890/220M, Chroma Technology, Bellow Falls, Vermont). In contrast, in the stimulated Raman gain detection scheme (Figure 1 b, c), the pump beam is modulated at 10.4 MHz and the transmitted Stokes beam is detected using a 4 mm^2 InGaAs photodetector with reversed bias of 10 V after filtering out the pump beam using a longpass filter (FEL1050, Thorlabs, Newton, New Jersey). Different detectors are chosen according to their wavelength-dependent responsivity.

Most images were taken using a stimulated Raman loss (SRL) setup (Figure 1 a) with a pixel dwell time of 40 or 120 μs depending on the signal strength. The imaging speed is mostly limited by the signal intensity. The pump beam intensity ranges from 40 to 140 mW and the Stokes beam intensity

ranges from 60 to 210 mW depending on the signal strength of the targeted species. Figure 3 g was taken using a stimulated Raman gain (SRG) setup (see Figure S1 of the Supporting Information), which will be discussed in detail in Section 2.4.

2.2. Assignment of Raman Resonance Peaks

Lipid, protein and nucleic acids are major biochemical components of a cell. They all have specific Raman peaks, many of which are within the fingerprint region. The vibrational modes used in this study are listed in Table 1.[18–26] The Raman peaks for nucleic acid, protein and lipid are confirmed using a confocal laser Raman spectrometer (Labram HR800, Horiba Jobin

Table 1. Raman peak assignment of different chemical bonds.

Raman peaks [cm^{-1}]	Functional group	Chemical species
783–790	symmetric phosphodiester stretch ring breathing modes of pyrimidine bases	nucleic acids
1090–1010	symmetric dioxy stretch of the phosphate backbone ν (C-C)	nucleic acids lipid
1655	amide I ν (C=O) ν (C=C)	protein unsaturated lipid
1004	phenylalanine	protein
2845	ν (CH2)	lipid

Yvon). Figure 2 a shows the Raman spectrum of a deoxyribonucleic acid (DNA) fiber extracted from salmon testes. The peak at 785 cm^{-1} originates from the superposition of the symmetric phosphodiester stretch and the ring breathing modes of the pyrimidine bases, and the peak at 1099 cm^{-1} originates from the symmetric dioxy-stretch of the phosphate backbone.[19] Figure 2 b shows the Raman spectrum of bovine serum albumin (BSA) powder which is a protein. The peak at 1004 cm^{-1} originates from the ring-breathing mode of phenylalanine in the protein.[26] Another peak at 1655 cm^{-1} originates from the Amide I band of the protein. Figure 2 c shows the Raman spectrum of oleic acid which represents unsaturated lipid. The peak at 2845 cm^{-1} originates from paraffinic C—H vibrations. Another peak at 1655 cm^{-1} originates from the C=C vibrations of unsaturated lipids, which overlaps with the Amide I band of protein. The peak at 1084 cm^{-1} originates from the skeletal C-C vibrations which may interfere with the 1099 cm^{-1} peak of nucleic acids. These peaks are within the range of those observed previously (See Table 1).

2.3. SRS Imaging of Single Polytene Chromosomes in the Salivary Gland Cells of Drosophila Melanogaster

Since the Raman signal of nucleic acids is very weak compared to that of lipids and proteins, the first cellular system in this study is the salivary gland cells in Drosophila melanogaster larvae because of their unusually high DNA concentration:
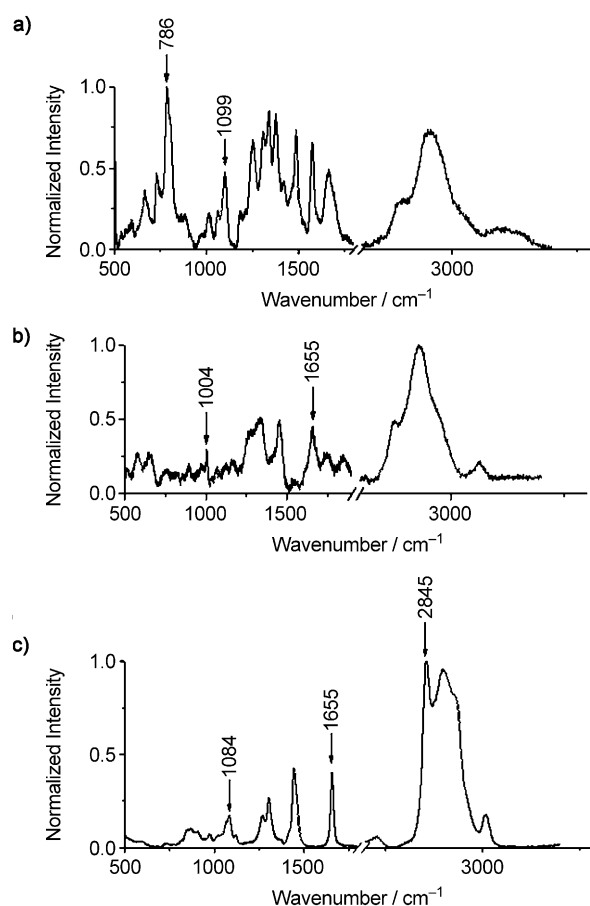

Figure 2. Raman spectra of: a) DNA, b) BSA, and c) oleic acid.

each cell contains 100–500 DNA copies. Based on the spontaneous Raman spectra from these cells (Figure 3 a), four peaks were selected for SRS imaging: 1) the peak at 2845 cm^{-1} attributed to the CH$_2$ vibration in lipids, 2) the peak at 1655 cm^{-1} attributed to the amide I band of proteins and 3) and 4) two peaks in the fingerprint region that are attributed to nucleic acids being the resonance at 785 cm^{-1} and 1090 cm^{-1} (see Table 1).

Figures 3 b–f show SRS images of the salivary gland cells of Drosophila melanogaster larvae at different Raman resonances. The image at 2845 cm^{-1} shows small lipid droplets that are visible as bright dots. The nucleus shows up as a dark zone due to its lack of lipids. The amide I channel measured at 1655 cm^{-1} shows a more homogeneous distribution since both the nucleus and the cytoplasm contain a large amount of protein. However, the C=C vibration in unsaturated lipid also has contribution to this channel due to its Raman peak at 1655 cm^{-1} (see Table 1). The bright dots in this channel mainly come from the lipid droplets in the cytoplasm.

The specific structure of the polytene DNA in the nucleus, which consists of multiple copies of tightly bound sister chromosomes, shows up at 785 and 1090 cm^{-1}. The typical banding structure called "puffing"[27] is clearly resolved (see Figure S2 of the Supporting Information). The specific structure arises from transcriptionally inactive, compacted regions of the
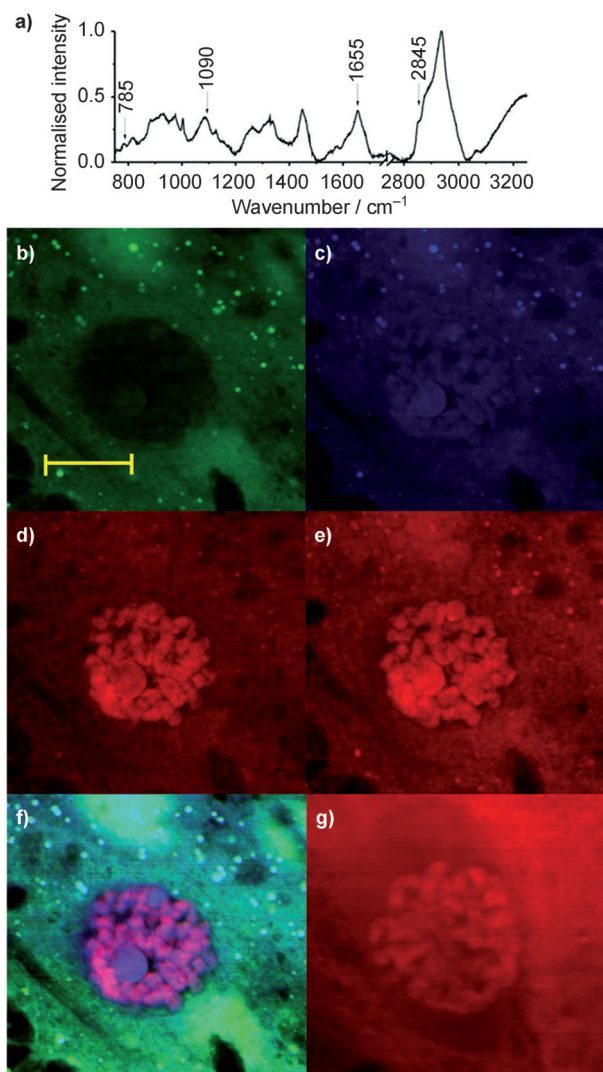
Figure 3. a) Raman spectrum of a Drosophila cell. b–g) SRS images of a salivary gland cell from Drosophila melanogaster, via the stimulated Raman loss detection scheme. b) Lipid-specific image taken at 2845 cm^{-1}, c) Amide I band at 1655 cm^{-1}, d) nucleic acids at 785 cm^{-1} and e) 1090 cm^{-1}. f) Multicolor image generated by combining images (b)–(e). g) Nucleic acid map recorded at 785 cm^{-1} via the stimulated Raman gain detection scheme. The scale bar is 20 μm. Each image has the size of 512×512 pixels.

this possibility by comparing images taken with the SRL and SRG detection schemes. XPM could contribute to the signal when the modulated Stokes beam intensity causes a modulation in the refractive index in focus due to the Kerr effect, therefore resulting in a modulation of the divergence of the transmitted pump beam. This divergence modulation can be transformed into amplitude modulation when the detection numerical aperture (NA) or the detector size is limited. In that case, it will be detected as a modulated loss in pump beam intensity. Obviously the signal size would depend on the detection geometry and becomes more significant when the detection NA is too small. In addition, the phase of the signal should be the same in both the SRL and the SRG detection configurations. Therefore XPM shows a positive signal in SRL but a negative signal in SRG. This allows us to distinguish XPM from the SRS signal. This phenomenon is confirmed by placing a pinhole in front of the detector to reduce the collection NA and measuring the XPM signal from water (off resonance of the O—H stretching vibration at 2830 cm^{-1}).[29] By closing down the pinhole, the XPM signal increases in phase with the pump beam in SRL but out of phase with the Stokes beam in SRG.

Figure 3 g shows SRG images taken in the salivary gland cells of Drosophila larvae. As discussed above, XPM should in principle show a negative signal in the SRG detection scheme. However, there is still a positive background signal in the cytoplasm. We therefore conclude that the background in the cytoplasm comes mainly from the Raman signal of RNA and the Raman background from other species, and not from XPM.

The merged image of the lipid, protein and nucleic-acid channels (Figure 3 f) shows a strong correlation between nucleic acids and protein resulting in a pink-colored polytene chromosome in which proteins not only serve as organizational units, but also fulfill an important function in gene transcription and other nuclear processes.

2.4. Determining the Cell Cycle Phase of Mammalian Cells Using SRS Imaging

Having demonstrated the detectability of single polytene chromosomes using SRS imaging, the technique was also applied to single mammalian cells that have a much lower DNA concentration. Based on the spontaneous Raman spectra of HEK293 cells (Figure 4 a), three peaks were selected at 2845, 785, and 1090 cm^{-1} for imaging lipids and nucleic acids (as in Section 2.3). To image the protein distribution, a different peak was selected at 1004 cm^{-1}, since there is interference at 1655 cm^{-1} from unsaturated lipid (as discussed in Section 2.3). The peak at 1004 cm^{-1} is attributed to the ring-breathing mode of phenylalanine.

Figure 4 shows the SRS biomolecular maps of HEK-293 cells. The same dark zone as shown before is observed in the nucleus at 2845 cm^{-1} (the lipid channel in Figure 4 a), and lipid droplets are visible in the cytoplasm. The protein channel shows signal in both the nucleus and the cytoplasm (Figure 4 c). Figures 4 d,e show that we can detect nucleic acids which are enriched in some cell nuclei. However, cell-to-cell variation is observed. The signal level is 2–5 times lower than
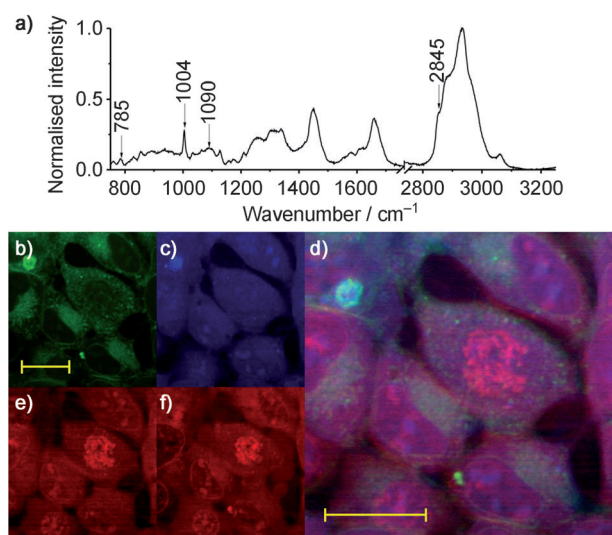
chromosome called heterochromatin and gene-rich transcriptionally-active regions of the chromosome called euchromatin. Heterochromatin has higher DNA concentration compared to euchromatin. It is worth noting that the fingerprint region of Raman spectra consists of several closely packed vibrational resonances. It is also reflected in our SRS images. For example, the 1090 cm^{-1} peak is amidst the abundant C-C vibrational resonance. This could explain the elevated signal in the lipid droplets in the cytoplasm. However, there is no contribution from C—C in 785 cm^{-1}, but there is still a background signal in the cytoplasm in this channel. This signal can, at least in part, be attributed to the presence of large amounts of RNA because of the similarity between DNA and RNA Raman spectra.

One likely imaging artifact, cross-phase modulation (XPM),[28, 29] could also give rise to this signal, but we ruled out

Figure 4. a) Raman spectrum of an HEK-293 cell pellet. b–f) SRS images of HEK-293 cells at: b) 2845 cm^{-1}, primarily lipid, c) 1004 cm^{-1}, phenylalanine, d) 785 cm^{-1}, nucleic acid, e) 1090 cm^{-1}, primarily nucleic acid. f) Multicolor overlay of (b)–(d). The scale bar is 20 μm.

that in salivary gland cells. Similar biomolecular maps are also observed in another mammalian cell line (MCF-7) (Figure 5). Fluorescent staining of DNA using a live cell dye was used to confirm that the nucleic acid enrichment in the nucleus correlated with an enrichment of dye labeled DNA (Figure S3 of the Supporting Information). Furthermore, the specificity of the signal was demonstrated by imaging 15 cm^{-1} away from the resonant peak (Figure S4, Supporting Information).

The cell-to-cell variations observed in the nucleic-acid channel are attributed to differences between metaphase cells and interphase cells. When the cell is in the interphase (Figure 5 a–d), there is an increased signal in the nucleolus, a region within the nucleus with high levels of ribosomal RNA production and hence a higher nucleic-acid concentration. It is also possible to observe when the cell is undergoing stages of cell division. For example, some cells show increased contrast within the nucleus (Figure 4 d,e) because they are in the prophase (the stage at which DNA condenses before cell division). Some cells show an increased signal lining up along one axis of the nucleus (Figure 5 g) and are in the metaphase (the stage at which condensed chromosomes line up in the middle of the cell before they separate into daughter cells). Such information allows us to distinguish cells that are dividing from cells that are not.

3. Conclusions

We have demonstrated that SRS microscopy can be used as a non-invasive label-free imaging tool for the quantitative mapping not only of protein and lipid distributions but also of nucleic-acid distributions. The SRS images of different cellular components have been shown in single salivary gland cells of Drosophila larvae, as well as in single HEK293 and MCF7 cells. We detected differences in the nucleic-acid signal when com-
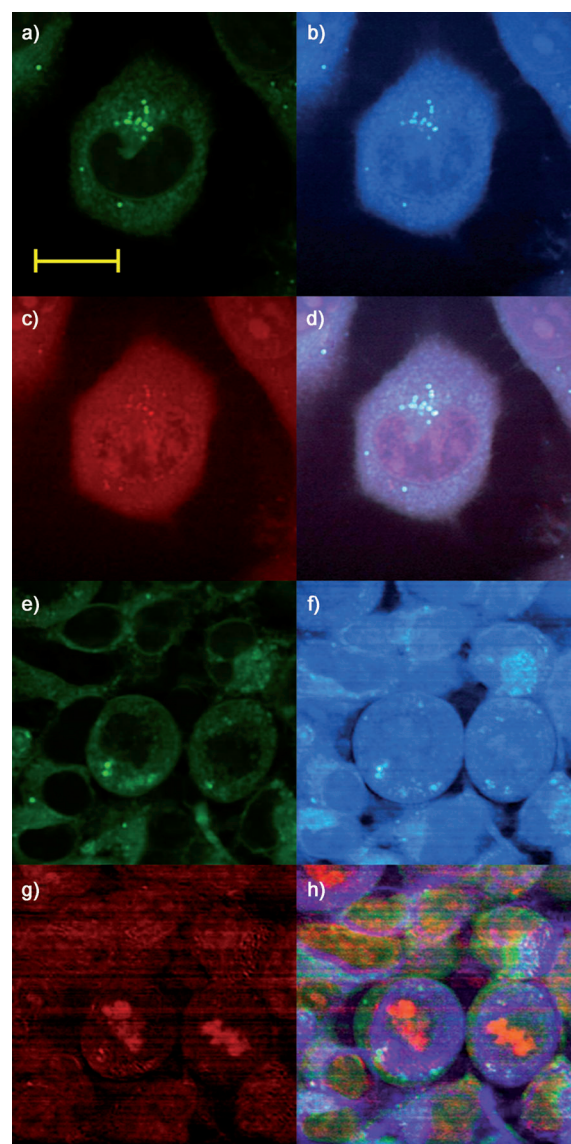

Figure 5. SRS images of MCF-7 cells at: a) 2845 cm^{-1}, primarily lipid, b) 1655 cm^{-1}, primarily protein, c) 785 cm^{-1}, nucleic acid, and d) overlay of (a)–(c). SRS images of a few other MCF-7 cells at: e) 2845 cm^{-1}, f) 1655 cm^{-1}, g) 785 cm^{-1}, and h) overlay of (e)–(g). The scale bar is 20 μm.

paring heterochromatin and euchromatin within these cells. In the case of the fruit fly, we demonstrated that we can detect the banding pattern of polytene chromosomes that is known to arise from alternating regions of heterochromatin and euchromatin. In the case of mammalian cells, we determine whether or not a cell is dividing through the detection of a nucleolus present in non-dividing cells during the interphase and the increased levels of DNA condensation that occur in dividing cells. Herein, we show that it is possible to detect cell division through imaging of DNA. This technique may be important in identifying cells undergoing cell division or apoptosis within living tissue, making it possible to study diseases such as cancer.

Experimental Section

Sample Preparation

MCF7 and HEK-293 cell lines (ATCC) are maintained at 37 °C in a humidified 5 % CO_2 air incubator. HEK-293 cells are cultured in DMEM (Invitrogen) supplemented with 10 % fetal bovine serum (Sigma). MCF7 cells are cultured in MEM (Invitrogen) supplemented with 10 % fetal bovine serum and 0.01 mg mL^{-1} insulin (Sigma). Cells are imaged in phenol red-free growth medium. Polytene chromosomes in Drosophila salivary glands were imaged directly in live fly larvae. The samples are placed between a mounting glass slide and a No. 1 coverslip (VWR, Radnor, Pennsylvania) and sealed with nail polish. The experiments were performed at room temperature.

Spontaneous Raman Spectroscopy

The spontaneous Raman spectra were acquired using a confocal laser Raman spectrometer (Labram HR800, Horiba Jobin Yvon) at room temperature. A 10 mW 633 nm HeNe laser was used to excite the sample through a 50×, 0.75 NA objective (MPlan N, Olympus). A polychromator with 600 lines per mm was used to disperse the light onto the CCD camera. The total data acquisition was performed during 40 seconds and the background was subtracted using the LabSpec software.

Acknowledgements

[1] N. Uzunbajakava, A. Lenferink, Y. Kraan, E. Volokhina, G. Vrensen, J. Greve, C. Otto, *Biophys. J.* **2003**, *84*, 3968 – 3981.

[2] G. J. Puppels, F. F. M. de Mul, C. Otto, J. Greve, M. Robert-Nicoud, D. J. Arndt-Jovin, T. M. Jovin, *Nature* **1990**, *347*, 301 – 303.

[3] C. Krafft, B. Dietzek, J. Popp, *Analyst* **2009**, *134*, 1046.

[4] K. Fujita, N. I. Smith, *Mol. Cells* **2008**, *26*, 530 – 535.

[5] R. J. Swain, M. M. Stevens, *Biochem. Soc. Trans.* **2007**, *35*, 544.

[6] A. Zumbusch, G. R. Holtom, X. S. Xie, *Phys. Rev. Lett.* **1999**, *82*, 20.

[7] C. L. Evans, E. O. Potma, M. Puoris'haag, D. Côté, C. P. Lin, X. S. Xie, *Proc. Natl. Acad. Sci. USA* **2005**, *102*, 16807.

[8] C. L. Evans, X. S. Xie, *Annu. Rev. Anal. Chem.* **2008**, *1*, 883 – 909.

[9] H. A. Rinia, M. Bonn, M. Müller, *J. Phys. Chem. B* **2006**, *110*, 4472 – 4479.

[10] F. Ganikhanov, C. L. Evans, B. G. Saar, X. S. Xie, *Opt. Lett.* **2006**, *31*, 1872 – 4.

[11] E. Ploetz, S. Laimgruber, S. Berner, W. Zinth, P. Gilch, *Appl. Phys. B* **2007**, *87*, 389 – 393.

[12] C. W. Freudiger, W. Min, B. G. Saar et al., *Science* **2008**, *322*, 1857.

[13] Y. Ozeki, F. Dake, F. S. Kajiyama, K. Fukui, K. Itoh, *Opt. Express* **2009**, *17*, 5.

[14] P. Nandakumar, A. Kovalev, A. Volkmer, *New J. Phys.* **2009**, *11*, 033026.

[15] B. G. Saar, C. W. Freudiger, J. Reichman, C. M. Stanley, G. R. Holtom, X. S. Xie, *Science* **2010**, *330*, 1368.

[16] M. Okuno, H. Kano, P. Leproux, V. Couderc, J. P. R. Day, M. Bonn, H. Hamaguchi, *Angew. Chem.* **2010**, *122*, 6925 – 6929; *Angew. Chem. Int. Ed.* **2010**, *49*, 6773 – 6777.

[17] I. Notingher, *Expert Rev. Med. Devices* **2006**, *3*, 215 – 34.

[18] G. J. Thomas, Jr., B. Prescott, D. E. Olins, *Science* **1977**, *197*, 385 – 388.

[19] D. C. Goodwin, J. Brahms, *J. Nucl. Acids Res.* **1978**, *5*, 835 – 850.

[20] J. M. Benevides, G. J. Tohomas, *Nucl. Acids Res.* **1983**, *11*, 5747 – 5761.

[21] B. Prescott, W. Steinmetx, G. J. Thomas, Jr., *Biopolymers* **1984**, *23*, 235 – 256.

[22] R. Savoie, J.-J. Jutier, S. Alex, P. Nadeau, P. N. Lewis, *Biophys. J.* **1985**, *47*, 451 – 459.

[23] G. J. Thomas, *Annu. Rev. Biophys. Biomol. Struct.* **1999**, *28*, 1 – 27.

[24] F. S. Parker, *Applications of Infrared, Raman and Resonance Raman Spectroscopy in Biochemistry* (Ed.: Frank S. Parker), Plenum Press, New York, **1983**.

[25] J. D. Gelder, K. D. Gussem, P. Vandenabeele, L. Moens, J. Raman, *Spectroscopy* **2007**, *38*, 1133 – 1147.

[26] M. B. J. Roeffaers, X. Zhang, C. W. Freudiger, B. G. Saar, M. Ruijven, G. Dalen, C. Xiao, X. S. Xie, *J. Biomed. Opt.* **2011**, *16*, 1 – 6.

[27] M. Ashburner, *Chromosoma* **1972**, *38*, 255 – 81.

[28] K. Ekvall, P. van der Meulen, C. Dhollande, L. E. Berg, S. Pommeret, R. Naskrecki, J. C. Mialocq, *J. Appl. Phys.* **2000**, *87*, 2340.

[29] C. W. Freudiger, M. B. J. Roeffaers, X. Zhang, B. G. Saar, W. Min, X. S. Xie, *J. Phys. Chem. B* **2011**, *115*, 5574 – 5581.